Cells Segmentation From 3-D Confocal Images of Early Zebrafish Embryogenesis

Cecilia Zanella, Matteo Campana, Barbara Rizzi, Camilo Melani, Gonzalo Sanguinetti, Paul Bourgine,
Karol Mikula, Nadine Peyriéras, and Alessandro Sarti

Abstract—We designed a strategy for extracting the shapes of cell membranes and nuclei from time lapse confocal images taken throughout early zebrafish embryogenesis using a partial-differential-equation-based segmentation. This segmentation step is a prerequisite for an accurate quantitative analysis of cell morphodynamics during embryogenesis and it is the basis for an integrated understanding of biological processes. The segmentation of embryonic cells requires live zebrafish embryos fluorescently labeled to highlight sub-cellular structures and designing specific algorithms by adapting classical methods to image features. Our strategy includes the following steps: the signal-to-noise ratio is first improved by an edge-preserving filtering, then the cell shape is reconstructed applying a fully automated algorithm based on a generalized version of the Subjective Surfaces technique. Finally we present a procedure for the algorithm validation either from the accuracy and the robustness perspective.

Index Terms—Bioimaging, confocal imaging, image processing, segmentation, subjective surfaces.

I. INTRODUCTION

THE 3-D reconstruction of cellular shape is a crucial task for reaching an integrated understanding of biological processes leading to organism formation. Providing automated procedures for reconstructing the shape of all the cells of a living vertebrate embryo is far beyond the current state of art. Achieving such a goal would readily provide measurements for a large number of biological features including cell shape changes and deformation characteristic for cell differentiation and tissue morphogenesis. Cell shape segmentation is also essential to track cell divisions and help reconstructing the cell lineage tree and from that extract the cell proliferation rate in space and time. This kind of data is highly relevant to investigate stem cell populations, early steps of cancerogenesis and drug effects *in vivo*. Furthermore, the reconstruction of the cellular shape will provide relevant parameters to measure the variability between different individuals of the same species, opening the way for understanding the individual susceptibility to genetic diseases or response to treatments. In this context, our aim is to design an algorithm achieving an automated segmentation of nuclei and membranes from 3-D time-lapse imaging of live embryos engineered to express fluorescent markers. Although interactive methods have better performances (in terms of the percentage of objects correctly segmented), we expected to avoid the need for any manual intervention that becomes unrealistic when manipulating millions of objects. The segmentation technique has to be chosen according to the data features. Typically, 3-D images for living organism provide incomplete information such as objects with missing boundaries and the segmentation technique should deal with that. Many algorithms for the shape reconstruction have been developed by researchers worldwide, and exist almost as many segmentation methods as there are segmentation problems. The 2-D and 3-D automatic or semi-automatic nuclei segmentation has been covered in a number of previous works [1]–[10]. In a recent work, Padfield *et al.* [11] describe a set of methods designed to automatically segment nuclei in 2-D time-lapse images. The methods, based on level set segmentation, have been used to effectively extract the nuclear tracks and generate a schematic representation of cell cycle phases. An alternative strategy for identifying cell trajectories and studying the variation of cell shape has been recently proposed by [12]. The algorithm performs cell segmentation and tracking using texture-adaptive snakes and has been tested on both normal and autophagy cell image sequences. All the developed algorithms have proved to be very useful for nuclei segmentation, however, the reconstruction of the whole cell using membrane protein markers is almost an unexplored area. In a previous work by Sarti *et al.* [10] confocal microscopy images were processed to extract the shape of nuclei. However, in that case, the analyzed volumes were not acquired from a living organism but from pieces of fixed tissues. On the contrary, the analysis of biological processes during embryogenesis means analyzing the cells

C. Zanella, M. Campana, B. Rizzi, and A. Sarti are with DEIS, Bologna University, 40136 Bologna, Italy (e-mail: cecilia.zanella2@unibo.it; m.campana@unibo.it; barbara.rizzi@unibo.it; alessandro.sarti@unibo.it).

C. Melani is with the Facultad de Ciencias Exactas y Naturales, Buenos Aires University, C1428EGA Buenos Aires, Argentina, and also with DEIS, Bologna University, 40136 Bologna, Italy (e-mail: camilo@dc.uba.ar).

G. Sanguinetti is with the Instituto de Ingeniería Eléctrica, Universidad de la República, 11300 Montevideo, Uruguay, and also with DEIS, Bologna University, 40136 Bologna, Italy (e-mail: gsangui@fing.edu.uy).}

P. Bourgine is with the Centre de Recherche en Epistémologie Appliquée, CNRS,École Polytechnique, 75005 Paris, France (e-mail: bourgine@shs.polytechnique.fr).

K. Mikula is with the Department of Mathematics, Slovak University of Technology, 81368 Bratislava, Slovak Republic (e-mail: mikula@vox.svf.stuba.sk).

N. Peyriéras is with the CNRS-DEPSN, Institut de Neurobiologie Alfred Fessard, 91198 Gif sur Yvette, France (e-mail: nadine.peyrieras@iaf.cnrs-gif.fr).

Color versions of one or more of the figures in this paper are available online at http://ieeexplore.ieee.org.

This paper has supplementary PDF material available at http://ieeexplore.ieee.org, provided by the authors. The material is 7.4 MB in file size. The supplementary material contains one multimedia AVI format movie clip, which shows the surface evolution throughout the segmentation process, and a ZIP format archive, which includes the algorithm code that can be interactively used to segment confocal images.

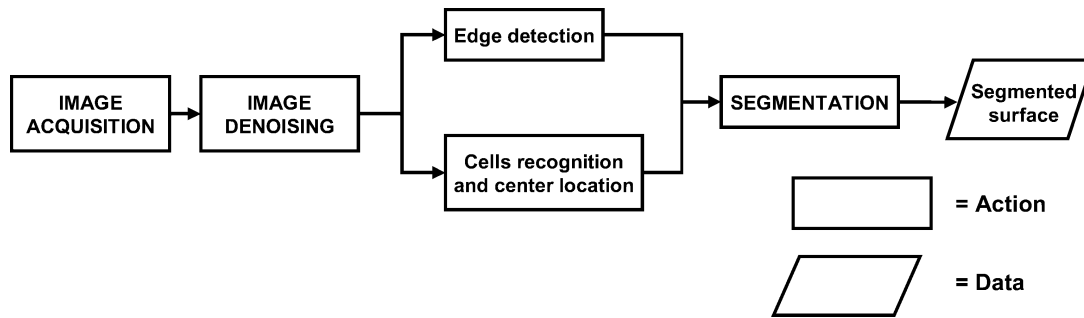Digital Object Identifier 10.1109/TIP.2009.2033629

Fig. 1. Flowchart depicting the sequence of steps we undertook for nuclei and membranes segmentation.

within their natural environment, i.e., in a living embryo. In that case, segmentation has to proceed from sequences of 3-D data whose quality is much more difficult to handle. In a recent work Keller *et al.* [1] developed digital scanned laser light sheet fluorescence microscopy for recording position and movements of zebrafish cell nuclei throughout the first 24 h of embryonic development. However, the reconstruction procedure does not deal with membranes image acquisition and shape reconstruction. Ortiz *et al.* [13] presented a segmentation algorithm based on gradient-curvature driven flow, which is suitable for whole cell segmentation. They measured the robustness against noise and resistance to surface discontinuities on synthetic images and demonstrated the suitability of the method on real cell images. However, as they discussed, the resistance to surface discontinuities is strictly dependent on a parameter introduced in curvature term that determines the strength of the regularization. This pose a trade-off choice between surface accuracy and missing boundaries filling that should be solved by the user. Here we present a method to segment a large number of cells from 3-D images characterized by non homogeneous intensity and gradient signal and capable to complete surface discontinuities without any compromise between precision and ability to integrate the incomplete contours. The segmentation method we propose in this work is a generalized version of the Subjective Surfaces technique [14], [16]: It is distinguishable from the classic formulation by the different weights applied on the two flows constituting the motion equation (curvature and advection). In addition, two different dynamics constitute the same segmentation process: By acting on the matching of level curves, we control the evolutive behavior in order to make it first mostly diffusive then a level set motion. In the biological application we deal with, these strategies are fundamental for reaching satisfactory results, as preliminarily shown in [17]. Here, we expose more widely the same base concepts, but including a study on the stability condition, an algorithm validation and an overview on future developments. The different sections of this paper follow the steps undertaken to acquire and analyze the 3-D confocal images (Fig. 1). In Section II, we briefly explain the technique for image acquisition. In Section III, we apply a filtering method for image denoising. In Section IV we describe the segmentation algorithm. Results are provided and discussed in Section V. Finally, in Section VI, we propose a strategy for the algorithm validation reporting its accuracy and robustness performances.

II. IMAGE ACQUISITION

A. In Vivo Imaging Technique

In vivo imaging is becoming an increasingly powerful tool for the analysis of morphodynamical patterns in biology. Microscopic imaging, taking advantage of fluorescent proteins engineering, is able to achieve a resolution at the sub cellular level in a whole living organism, to analyze biological circuits dynamics and quantify molecular components. To obtain accurate measurements of 3-D features at the cellular level in living embryos, it is necessary to use an acquisition technique with micrometrical resolution, able to reconstruct volumetric information and with enough contrast to allow segmentation of individual cells. To fulfill these requirements, the analyzed images have been acquired by *confocal microscopy (CLSM)* or by *multiphoton laser scanning microscopy (MLSM)* with the best compromise in terms of spatial and temporal resolution [18]. *LSM (laser scanning microscopy)* converts the fluorescent radiation coming from a point of the excited sample into a proportional electrical signal. Repeating the scan for all the points belonging to the focal plane, it is possible to reconstruct the image of a sample section and, varying the depth of the plane, an entire volume can be acquired. The acquisition repeated for a temporal series turns a sequence of tridimensional data into a 4-D data set. In order to produce high contrast images, the specimen has been labeled through the expression of fluorescent proteins: *eGFP* (enhanced Green Fluorescent Protein, targeted to nuclei) and *mCherry* (a Red Fluorescent Protein, addressed to the membranes). This procedure produces high contrast images containing high intensity regions, where a labeled structure is acquired, versus low intensity background regions. The two channels were acquired separately but simultaneously, as the emission spectrum of the two proteins are sufficiently distinct.

B. Data

Our animal model is the zebrafish (*Danio rerio*). This is a vertebrate that has been largely validated as a powerful model for investigations related to human, including cancerogenesis and a number of genetic diseases [19], and might become soon a major model organism for preclinical drug testing by pharmaceutical industries. A huge advantage of zebrafish is its suitability for *in vivo* imaging: the embryos are transparent, small and they develop outside the mother. This means that a zebrafish egg can
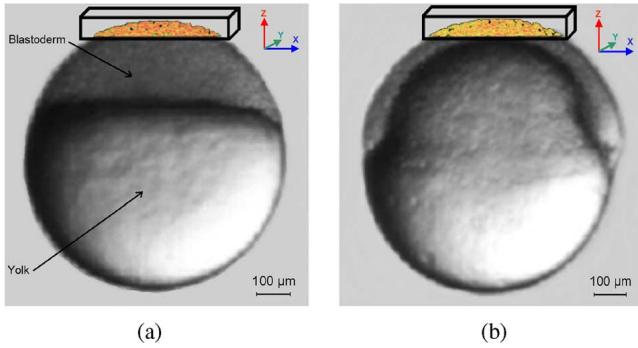
Fig. 2.   Acquired portion of the Zebrafish embryo: (a) start point about 3 h post fertilization, (b) end point about 7 h post fertilization.

be continuously imaged throughout embryogenesis. The x, y, z size of the acquired images was $512 \times 512 \times 30$ voxels. The axial (z) resolution is around 2-fold less than the planar (xy) resolution, so the volumetric images are nonuniform in spacing: the voxels size is 0.58 μm in x and y directions and 1.04 μm in z. The overall volume submitted to optical sectioning is about 30 microns thick. The embryo has been imaged from 3 h post fertilization, the time lapse goes on for a period of time T of 4 h, with a temporal resolution ΔT of about 5 minutes. As the morphogenesis is slowed down by the temperature (about 23°C), by the end of the time lapse the embryo is just starting gastrulation (6 h of development at 28°C) [20]. Fig. 2 shows the acquired portion in the entire animal volume. The volume that has been imaged encompasses part of the *blastoderm* (the embryonic cell mass) and does not get into the *yolk* (the noncellular mass of nutrients).

III. IMAGE DENOISING

The noise present in the image can disrupt the shape information, therefore denoising is an essential preliminary task in images segmentation. Noise has different sources such as photon noise, non homogeneous concentration of fluorescent proteins in the labeled structures or the electronic noise from the instrument. In order to accurately reconstruct the object shape, the denoising method has to improve the signal-to-noise ratio, faithfully preserving the position of the boundaries that define the shape of the structures.

We then chose to filter the data with the so called *geodesic curvature filtering* [10] which has been proved to be suitable for this kind of dataset [21], [22].

Besides this, membranes segmentation requires an additional preprocessing. Membranes images are corrupted by a weak nuclei signal, more intense during mitosis. This is due to overlapping between nuclei and membranes emission range during acquisition. A preliminary thresholding of nuclei images separates the nuclei signal from the background, highlighting the interfering signal that is then subtracted from the membranes images. This simple procedure prevents a wrong interpretation of the membranes edges deriving from the crosstalk between the two fluorescent signals.
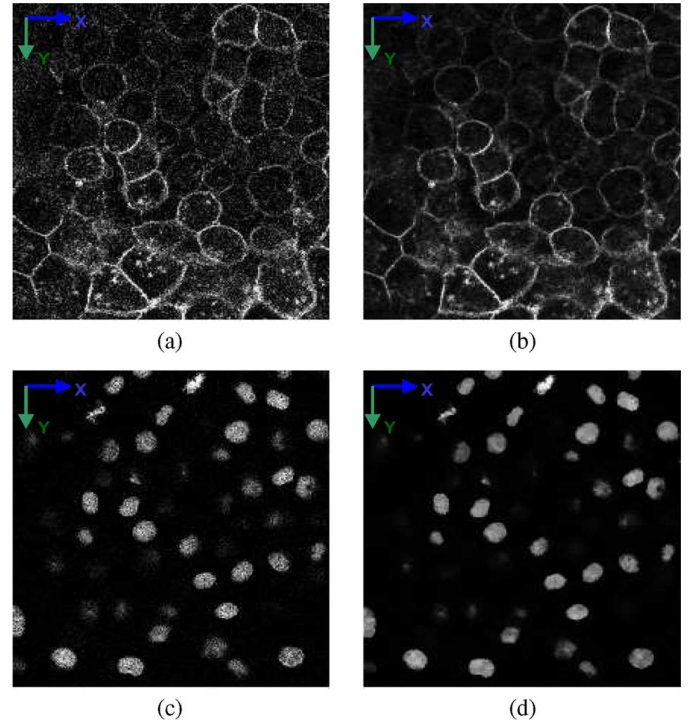

Fig. 3.   Details of filtering results (on the right) in comparison with the original images (on the left) for membranes (a), (b) and nuclei (c), (d) xy slices. The noise is greatly reduced and the image contrast is enhanced thanks to the intensity level sets accumulation around the boundaries promoted by the geodesic curvature technique. Gray level images with values 0 (black) and 255 (white).

IV. ALGORITHM FOR CELL SEGMENTATION

This section presents a detailed description of the steps undertaken in our segmentation algorithm. We particularly focus on membranes images, that are typically characterized by a low or even absent signal, giving rise to incomplete contours. Missing boundaries could be completed by using the Geodesic Active Contour method [23], but the technique greatly depends on the algorithm initialization: at the starting point, the reference level has to be an approximation of the final contour. An interesting solution, that does not require any *a priori* knowledge about the edges topology, has been introduced in [9] and consists in the use of a Malladi-Sethian approach [24]. Every membrane is segmented using a level-set function initialized in its center and then expanded by a balloon term. The missing boundaries are completed by a manually chosen different weight between the regularization and expansion term. Anyway, as we are dealing with thousands of cells, the user intervention is, in our case, unfeasible. Moreover, if the weight term is automatically chosen, the method is often not able to correctly detect the membranes boundaries. We propose to use a different technique, based on the Subjective Surfaces [14], [16] model, in order to correctly reconstruct the shape of membranes without any manual intervention. The Subjective Surfaces method has been introduced [14] to segment objects characterized by a wide absence of information on boundaries. Such peculiarity makes the model suitable especially for this particular application. Besides, we would like
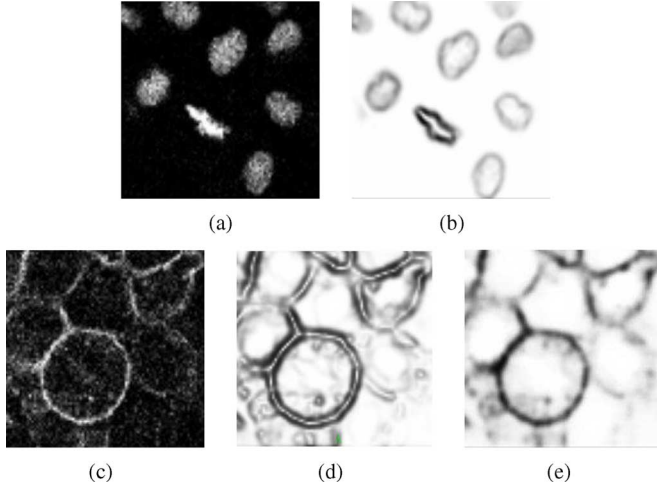
(a)   (b)

(c)   (d)   (e)

Fig. 4. Details of (a) nuclei and (c) membranes original data and the edge indicators obtained by applying the standard formulation of g, (b) and (d), respectively; (e) is the alternative edge indicator defined in order to detect a single contour in membranes images. Images (a), (c) with a color map from 0 (black) to 255 (white) depicting original data intensity. In images (b), (d), and (e), colors map values of the edge indicators from 0 (black) to 1 (white).

to point out that the Subjective Surfaces can be successfully applied also to nuclei segmentation, automatically solving problems related to nuclei sometimes clustered as the microscope resolution is not able to distinguish them.

The proposed procedure requires two preliminary steps: a low level image features extraction, illustrated in Section IV-A, and the detection of cells position, presented in Section IV-B. The section proceeds with a detailed description of the Subjective Surfaces algorithm and is concluded by the numerical scheme used for discretization.

A. Low Level Features Extraction: Edge Detector

The initial task of the segmentation strategy is to extract the so-called low level image features. For such purpose a classic solution is to consider an edge indicator $g = g(x, y, z)$, a smooth nonincreasing function of the image gradient [25]

$$g(x, y, z) = \frac{1}{1 + (|\nabla G_\sigma(x, y, z) * I(x, y, z)| / \beta)^n} \quad (1)$$

where $G_\sigma(x, y, z)$ is a Gaussian kernel with standard deviation σ, $*$ denotes the convolution, $I = I(x, y, z)$ represents the filtered imaged, and n is typically 1 or 2. The parameter σ determines the minimal size of details that can be preserved, whereas β is related to the image contrast and acts as a scale factor by which the image gray levels are mapped into the g function.

The value of g is close to 1 in flat areas ($|\nabla I| \to 0$) and close to 0 in the regions where image gradient is high (i.e., edges). Thus, the minima of g denote the position of the edges and its minus gradient is a force field that can be used to drive the evolution, because it always points in the local edge direction. The analyzed signals (membranes versus nuclei) behave in a completely different way in terms of edge detection: nuclei are solid and well contrasted objects; membranes are hollow, with a thickness of about 3 to 4 voxels and adjacent to each other. In nuclei images, the contours to be segmented are located in the regions where image gradient is higher and the minima of
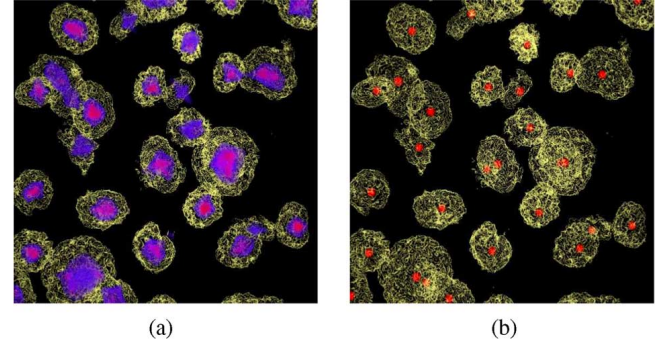

(a)   (b)

Fig. 5. Example of application of the Hough transform on nuclei images: (a) volume rendering representation of the nuclei channel (yellow) and the accumulator array; (b) detected centers, a red sphere is rendered everywhere the Hough transform recognizes a nucleus.

(1) denote the position of the edges [Fig. 4(b)]. On the contrary, the function (1) reveals a double contour, on the internal and the external side of cells [Fig. 4(d)]. These specific features require using different functions for the detection of the edges in nuclei and membranes images. In order to locate the minima of g in the middle of membranes thickness, we propose an alternative edge indicator, using the image itself (not its gradient) as a contours detector. The edge indicator we propose is

$$g(x, y, z) = \frac{1}{1 + (|G_\sigma(x, y, z) * I(x, y, z)| / \beta)^n} \quad (2)$$

as expected, its minima locate the contours in the middle of the membranes thickness [Fig. 4(e)].

B. Selection of a Point of View: Cells Recognition and Location

The second step in the segmentation procedure consists in finding a reference point located in the center of the object to segment. Observing that nuclei are always surrounded by membranes, we use the nuclear centers as starting points to segment both, nuclei and corresponding membranes. The nuclei localization is achieved with the *generalized 3-D Hough transform* [26] that allows detecting specific shapes within an image. By approximating the nucleus as a spherical object, the Hough Transform is able to recognize every nucleus and to provide its center [27]. Before applying the Hough transform, the volumes are transformed into an edge representation using the *Canny edge detection* algorithm [28] which has mainly three advantages that make it optimal as a preprocessing step of the Hough transform: it is able to locate and mark all real edges, it minimizes the distance between the detected edge and real edge and it produces only one response per edge. A sphere with center (x_0, y_0, z_0) and radius r is the set of points (x, y, z) where $(x - x_0)^2 + (y - y_0)^2 + (z - z_0)^2 = r^2$ and the parameters space of the spheres with a fixed radius is a 3-D space defined by (x_0, y_0, z_0). We also know that the center of a sphere is located r units from the point (x, y, z) in the direction of the image gradient in (x, y, z). The Hough transform accumulates in a 3-D array the votes of the edge points of the image [Fig. 5(a)]. The coordinates of those votes represent the parameters of the spheres that we are looking for. Therefore, coordinates with the highest value are most likely representing the parameters of a sphere in the image space and the center of each nucleus can be

recognized detecting the local maxima in the accumulator array [Fig. 5(b)]. To make the method more flexible, we consider a range of values for the sphere radius $[r_{\min}, r_{\max}]$ and a variation of the gradient direction. Thus, for each edge point (x, y, z) the sphere center is located in the neighborhood defined by the interval $[r_{\min}, r_{\max}]$ and by the angular sector along the gradient direction.

C. Segmentation: Modified Version of the Subjective Surfaces Technique

The method of Subjective Surfaces, as introduced in [16] and then improved in [15], consists, in the 3-D case, in the volume minimization of a 3-D manifold embedded in a 4-D Riemannian space with a metric constructed on the image itself. Let us consider the filtered image $\mathcal{I} : (x, y, z) \rightarrow I(x, y, z)$ as a real positive function in some domain $M \subset R^3$ and its low level local features given by the function $g = g(x, y, z)$ defined in Section IV-A. Such function is used to construct a Riemannian metric h in R^4 that will be used as embedding for a 3-D hypersurface evolution

$$h = \begin{pmatrix} g & 0 & 0 & 0 \\ 0 & g & 0 & 0 \\ 0 & 0 & g & 0 \\ 0 & 0 & 0 & g/a \end{pmatrix} \qquad (3)$$

starting from the center of object to be segmented (in our case nucleus center, see Section IV-B), an initial function $\Phi_0 = \Phi_0(x, y, z)$ is then constructed, in the image domain M, usually as a distance or peak function. Let us define $\Phi = \Phi(x, y, z, t)$ an evolution of Φ_0, where t represents a synthetic time known in literature as scale parameter. We point out that $\Phi(x, y, z, 0) = \Phi_0$. The graph of Φ represents a 3-D manifold $S = (x, y, z, \Phi)$ embedded in (R^4, h). Φ is evolved afterward by a mean curvature motion to minimize the volume of the hypersurface S through the following motion equation:

$$\Phi_t = H_g |\nabla \Phi|_a \qquad (4)$$

where

$$H_g = gH + (\nabla g \cdot \nabla \Phi) \frac{1}{|\nabla \Phi|_a} \qquad (5)$$

represents the mean curvature of S in (R^4, h) and

$$|\nabla \Phi|_a = \sqrt{a + |\nabla \Phi|^2} \qquad (6)$$

can be seen as a regularization of $|\nabla \Phi|$ [29]. In (5) H still represents a mean curvature for S, but with a metric h in which the edge detector g is equal to 1 [see (7), shown at the bottom of
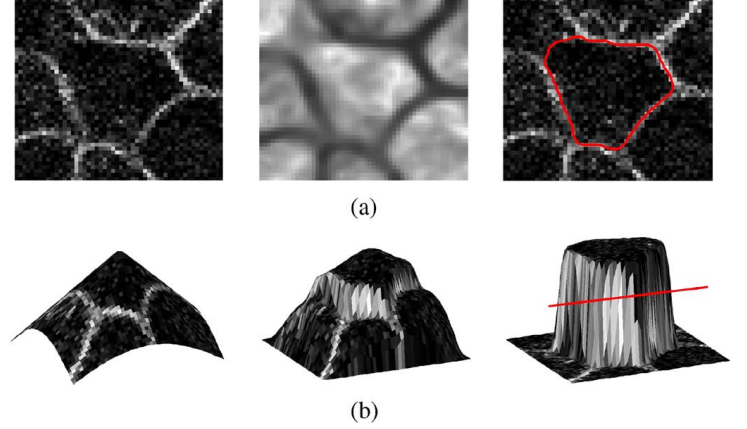

(a)

(b)

Fig. 6. Two-dimensional example of membrane segmentation in case of missing boundaries. (a, from left to right) Original data, edge detector, segmented contour, in red, superimposed to original data. (b, from left to right) Evolution of the initial point-of-view surface and selection of a level set, red line, for segmentation.

the page]. Subscripted denote shorthand notations for derivatives, i.e., $\Phi_t = \partial \Phi / \partial t$, $\Phi_x = \partial \Phi / \partial x$, $\Phi_{xx} = \partial^2 \Phi / \partial x^2$, $\Phi_{xy} = \partial^2 \Phi / \partial x \partial y$, and similarly for other spatial variables.

Let us now represent (4) in a more general formulation by adding two different weights, μ and ν, to the first and second term of the right side of (5). By considering boundaries and initial conditions, we can then write our model equation as follows:

$$\begin{cases} \Phi_t = \mu g H |\nabla \Phi|_a + \nu \nabla g \cdot \nabla \Phi, & \text{in } M \times]0, \tau[\\ \Phi(x, y, z, t) = \min(\Phi_0), & \text{in } \partial M \times]0, \tau[\\ \Phi(x, y, z, 0) = \Phi_0, & \text{for } (x, y, z) \in M \end{cases} \qquad (8)$$

where τ is the value of scale parameter t which corresponds to the steady state condition for (8).

Our model equation can then be read as in the following. The first term on the right side of (8) represents a mean curvature flow, a parabolic motion that evolves the hypersurface in normal direction with a velocity given by the mean curvature H and weighted by the edge indicator g. The second term is a pure passive advection along the velocity field $-\nabla g$, whose direction and strength depend on position. This term attracts the hypersurface in the direction of the image edges. Locally, different behaviors can be identified in the image regions according to one of these flows. In the homogeneous regions $g = 1$ and $\nabla g \rightarrow 0$; therefore, (8) reduces to the mean curvature flow: inside the objects the hypersurface levels collapse in a point then disappear. In regions where the edge information exists $g \rightarrow 0$ and (8) reduces to a simple advection equation: The hypersurface levels are driven towards the edges by the field $-\nabla g$, their accumulation causes the increase of the spatial gradient and S starts to generate discontinuities. In regions with subjective contours

$$H = \frac{\left(a + \Phi_x^2 + \Phi_y^2\right) \Phi_{zz} + \left(a + \Phi_x^2 + \Phi_z^2\right) \Phi_{yy} + \left(a + \Phi_y^2 + \Phi_z^2\right) \Phi_{xx}}{\left(a + \Phi_x^2 + \Phi_y^2 + \Phi_z^2\right)^{3/2}} - 2 \frac{\Phi_x \Phi_z \Phi_{xz} + \Phi_x \Phi_y \Phi_{xy} + \Phi_y \Phi_z \Phi_{yz}}{\left(a + \Phi_x^2 + \Phi_y^2 + \Phi_z^2\right)^{3/2}} \qquad (7)$$

(missing boundaries), continuation of existing edge fragments, a is negligible and (8) can be approximated by a geodesic flow, allowing the boundary completion with geodesics. The application of these dynamics is clear in Fig. 6, showing the effect of boundary completion in a membrane with a missing contour. The use of different weights between the regularization and the advective terms ($\nu > \mu$) facilitates the control of evolutive process. Indeed, the segmentation, together with the missing contours completion, is obtained through the shocks developed by the hypersurface on object boundaries, while the hypersurface is simultaneously smoothed and flattened inside the object. A higher weight of advective term ensures a better accumulation of image gray levels around existing contours. The parameter a introduced in the metric is a stretching factor and represents a weight between two different dynamics. It indeed shifts the model from the mean curvature flow of level sets ($a = 0$) to the mean curvature flow of graph ($a = 1$). We will show in Section V how we changed the a value in order to modify the dynamics of motion equation and to improve the segmentation of not perfectly centered objects.

D. Numerical Discretization

Concerning the numerical schemes for discretization, the partial derivatives in (8) are approximated with finite differences [14], [16], [30]. Time derivatives are discretized with first order forward differences, the parabolic term with central differences and the advective term with upwind schemes, where the direction of the one-sided difference used in a point depends on the direction of the vector field $v = -\nabla g$ in the same point. Let us consider a uniform grid in space-time (x, y, z, t), then the grid consists of the points $(x_i, y_j, z_k, t_n) = (i\Delta x, j\Delta y, k\Delta z, n\Delta t)$. We denote by Φ_{ijk}^n the value of the function Φ at the grid point (x_i, y_j, z_k, t_n), by g_{ijk} the value of the edge indicator in the grid point (x_i, y_j, z_k) and by v_{ijk} the value of the vector field v in the same spatial grid point. The numerical approximation of (8) is given by (9), shown at the bottom of the page, where D is a finite difference operator on Φ_{ijk}^n, the superscripts $\{-1, 0, 1\}$ indicate backward, central, and forward differences and the superscripts $\{x, y, z\}$ indicate the direction of differentiation.
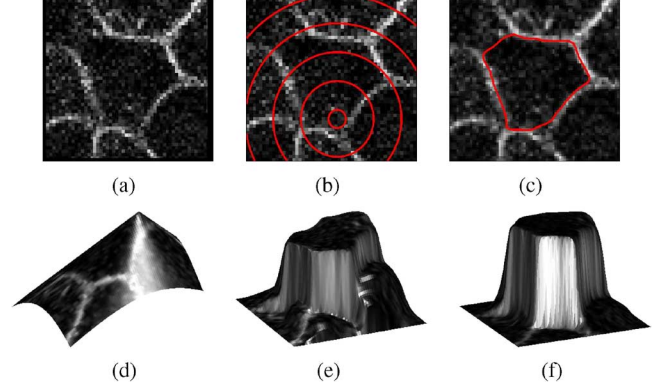

Fig. 7. Two-dimensional example of membrane segmentation in case of missing boundaries. The point for the Surface initialization is chosen very close to the boundaries but the membrane is correctly segmented thanks to the use of different values for the parameter a during the Surface evolution. (a) Original membrane. (b) Initial distance function Φ, depicted in red, superimposed on the original data. (c) Membrane segmentation, in red, superimposed on the original data. (d) Original Surface S constructed as graph of Φ. (e) The Surface at the end of the first, diffusive, process ($a = 1$). (f) The Surface at the end of the evolution, after a pure level set motion ($a = 10^{-6}$).

V. RESULTS AND DISCUSSION

We applied our algorithm to time-lapse 3-D datasets depicting zebrafish embryogenesis at cellular level. As reference points for the algorithm initialization we chose the cell nuclei centers detected via the generalized 3-D Hough transform. We then constructed an hypersurface in (R^4, h) by defining a Φ_0 function in the image domain M. We used $\Phi_0 = \alpha/\mathcal{D}$, where $\mathcal{D}$ is the 3-D euclidean distance from the reference point and α is a positive constant. The same expression of Φ_0 can be employed both for nuclei and membranes segmentation. Starting from the initialized surface, we performed nucleus/membrane segmentation by using the following values of parameters:

- high value of $a = 1$;
- low value of $a = 10^{-6}$;
- load of the curvature term $\mu = 0.1$;
- load of the advective term $\nu = 10$;
- time step $\Delta t = 0.065$.

In the conclusive step of the algorithm, we automatically picked the level set that describes the desired object. After segmentation, the intensity distribution of the function

$$\Phi_{ijk}^{n+1} = \Phi_{ijk}^n + \Delta t \left\{ \mu g_{ijk} \left[\frac{\left(a + D_{ijk}^{0_x^2} + D_{ijk}^{0_y^2}\right) D_{ijk}^{0_{zz}} + \left(a + D_{ijk}^{0_x^2} + D_{ijk}^{0_z^2}\right) D_{ijk}^{0_{yy}} + \left(a + D_{ijk}^{0_y^2} + D_{ijk}^{0_z^2}\right) D_{ijk}^{0_{xx}}}{a + D_{ijk}^{0_x^2} + D_{ijk}^{0_y^2} + D_{ijk}^{0_z^2}} + \right. \right.$$
$$\left. -2 \frac{D_{ijk}^{0_x} D_{ijk}^{0_z} D_{ijk}^{0_{xz}} + D_{ijk}^{0_x} D_{ijk}^{0_y} D_{ijk}^{0_{xy}} + D_{ijk}^{0_y} D_{ijk}^{0_z} D_{ijk}^{0_{yz}}}{a + D_{ijk}^{0_x^2} + D_{ijk}^{0_y^2} + D_{ijk}^{0_z^2}} \right]$$
$$-\nu \left\{ \left[\min\left(v_{ijk}^{0_x}, 0\right) D_{ijk}^{+x} + \max\left(v_{ijk}^{0_x}, 0\right) D_{ijk}^{-x} + \min\left(v_{ijk}^{0_y}, 0\right) D_{ijk}^{+y} + \max\left(v_{ijk}^{0_y}, 0\right) D_{ijk}^{-y} \right. \right.$$
$$\left. \left. \left. + \min\left(v_{ijk}^{0_z}, 0\right) D_{ijk}^{+z} + \max\left(v_{ijk}^{0_z}, 0\right) D_{ijk}^{-z} \right] \right\} \right\} \tag{9}$$
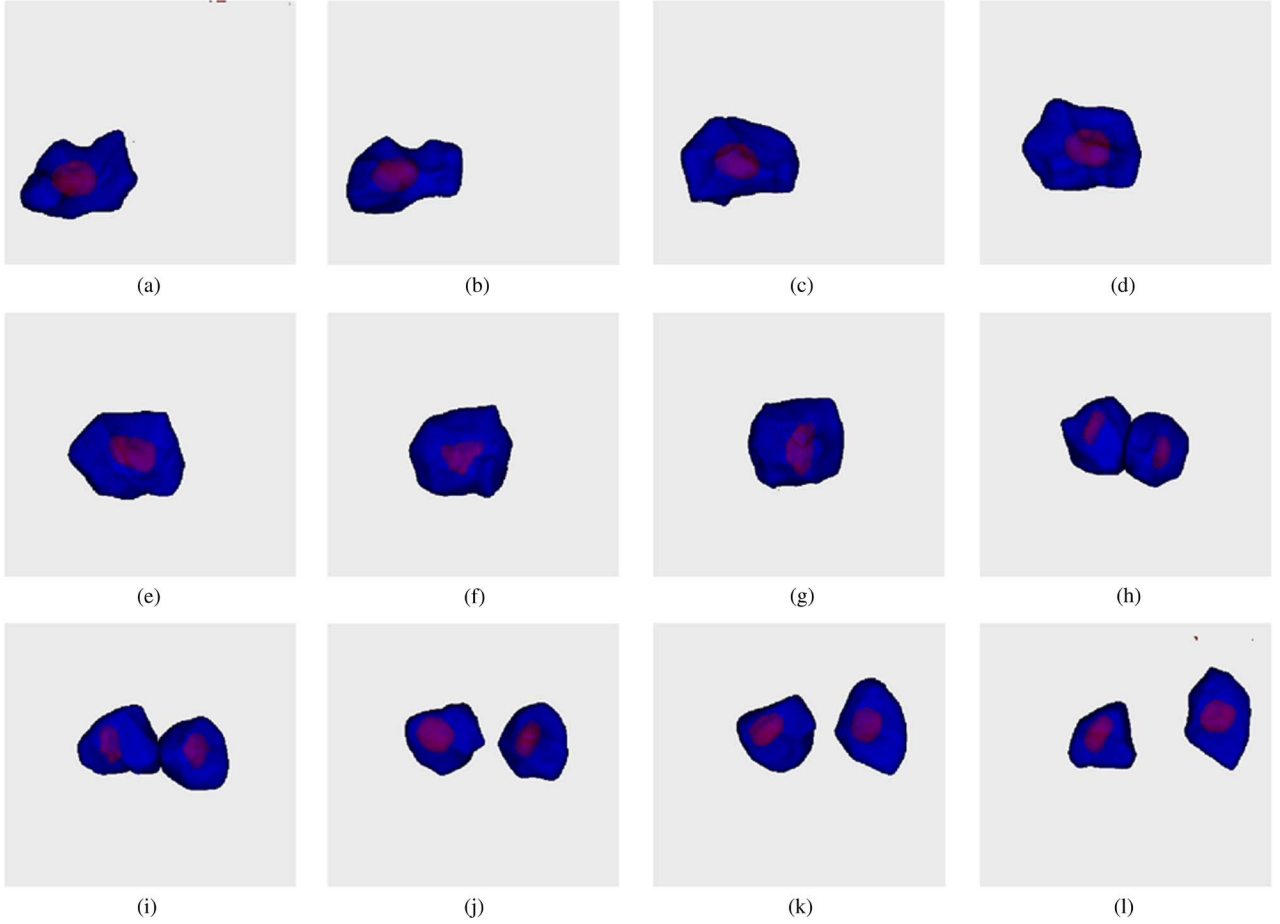
Fig. 8.   Sequence of cell division. (a) Step 1; (b) Step 2; (c) Step 3; (d) Step 4; (e) Step 5 (*Prophase*); (f) Step 6 (*Prometaphase*); (g) Step 7 (*Metaphase*); (h) Step 8 (*Telophase*); (i) Step 9; (j) Step 10 (*Cytokinesis*); (k) Step 11; (l) Step 12.

$\Phi_{\text{end}} = \Phi(x, y, z, \tau)$ is typically associated to a bimodal histogram. Therefore, the segmented surface could be extracted as the isosurface corresponding to the intermediate value of Φ_{end} scalar range.

Each object is processed separately from the others limiting the computation to subvolumes containing only one cell. This structure greatly simplifies the code parallelization, because it allows subdividing the volume in blocks of few cells, sending blocks to different processors for computation and then collecting all the segmented surfaces as a single result. The position of the reference point influences the result of segmentation. If it is around the object center, at the end of the evolution the highest hypersurface values correspond to the shape we want to extract. On the contrary, if we consider a strongly off-center reference point other adjacent structures may become predominant, not allowing a correct segmentation [16]. We solved this problem, at least partially, by changing the motion equation dynamics during the evolution process. Using first a high value of parameter a the process is mostly diffusive: the hypersurface smooths, moving away from the adjacent external structures, and simultaneously flattens inside the object. Then, with a low value of a, the hypersurface evolves driven by a pure level set motion, sharpening its discontinuities. A bidimensional example is shown in Fig. 7. Since diffusion was faster, the number of iterations with a high value of a was lower than the number

of iterations with a low value of a, to make comparable the effects of the two motions on the final contour. We used the same parameters both for nuclei and membranes processing, except for the total number of iterations: nuclei are smaller; thus, their segmentation requires less iterations (40000 iterative steps for membranes, 10000 for nuclei). The discrete time step Δt has been chosen as the maximum value which insures the stability of the advective term in (8). The stability condition, which can be deduced from mass balance considerations [31] applied to a single voxel, is given by

$$\frac{\Delta t}{\Delta x}|v_x| + \frac{\Delta t}{\Delta y}|v_y| + \frac{\Delta t}{\Delta z}|v_z| \le 1 \qquad (10)$$

where v_x, v_y, v_z are the velocity components. In our application we used the following approximation of the components arising in the velocity field

$$g_x \approx \frac{g_{i+1,j,k} - g_{i-1,j,k}}{2}$$

$$g_y \approx \frac{g_{i,j+1,k} - g_{i,j-1,k}}{2}$$

$$g_z \approx \frac{g_{i,j,k+1} - g_{i,j,k-1}}{2} \qquad (11)$$

since $0 \le g \le 1$, in the worst case $|g_x| = |g_y| = |g_z| = 0.5$. Therefore, substituting this value in (11) and setting $\Delta x = \Delta y = \Delta z = 1$, we obtain from (10) $\Delta t \le 2/3\nu$. In our case
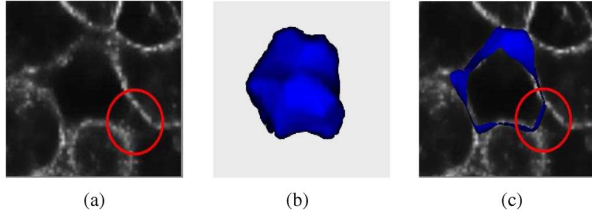
Fig. 9. Segmentation of a membrane with an uncompleted contour: (a) missing portion underlined by a red circle, (b) segmented surface, (c) cut of the surface superimposed on an image slice.
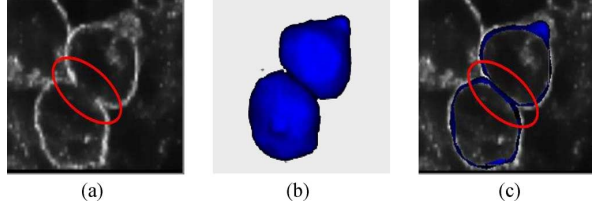

Fig. 10. Segmentation of a dividing cell: (a) constriction of the membrane underlined by a red circle, (b) segmented surface, (c) cut of the surface superimposed on an image slice.
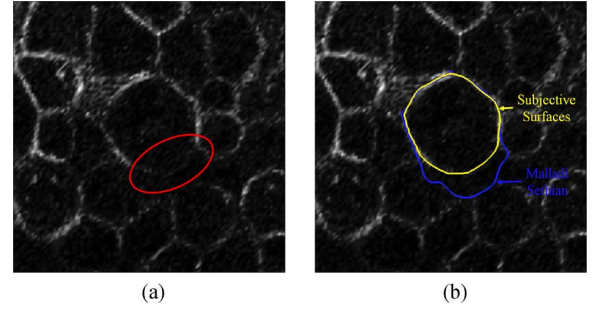

Fig. 11. Segmentation of an uncompleted membrane by using different segmentation techniques: (a) missing portion underlined by a red circle, (b) segmented contour (yellow line Subjective Surfaces, blue line Malladi-Sethian).
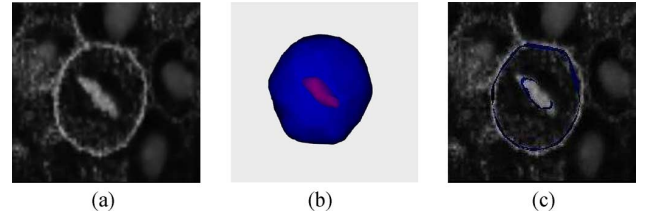

Fig. 12. Segmentation of a cell before division: (a) superimposition of membranes and nuclei signals, (b) segmented surfaces, (c) cut of the surfaces superimposed on an image slice.

$\nu = 10$, so we set $\Delta t = 0.065$. A similar analysis is difficult for the curvature term because it depends in nonlinear way on the solution. In the actual implementation we did not use strong curvature weight. In case of strong curvature influence one should approximate the equation through the semi-implicit schemes [32]–[35] which are unconditionally stable. In this section, we show some meaningful results of segmentation on two different cell types distinguishable in the imaged developmental period: *epithelial* cells from the enveloping layer and *inner* cells. Their morphology varies along the cell cycle introducing more morphological categories. The inner cell mass is covered by an epithelial layer (EVL or enveloping layer). EVL cells are polarized, i.e., their apical surface and baso-lateral surface have specific properties, polygonal, large, flat and they largely keep their shape when dividing. They sometime have several nuclei, due to some stress condition linked to manipulation. They also always show intracellular membrane staining, probably corresponding to intra cellular membrane compartments. Inner cells are smaller than EVL cells and not polarized. They fill the space and their nucleus is centered. During division inner cells become spherical and largely loose adhesion to their neighbors. Fig. 9 shows the effect of boundary completion on an inner cell: The missing contour, underlined by the red circle, is completed by a straight line. The algorithm shows the same behavior for dividing membranes (Fig. 10). When two different nuclei are found inside the same cell and the membrane presents a constriction along the division plane, the algorithm segments two cells by completing their contours with straight lines. These results demonstrate the suitability of the Subjective Surfaces technique for this scenario, especially if compared with other methods. In Fig. 11 we discuss our algorithm against Malladi-Sethian approach [24] in the specific case study of missing membrane boundary. The performances are comparable in the region with well defined contours, whereas the final shape achieved by the classical level set method fails in membrane completion. Before undergoing division, inner cells become spherical, whereas nuclei staining

elongates as the chromosomes arrange in the future cell division plane (Fig. 12). It should be noted that the nucleus size is underestimated in the last two parts. This is due to the parabolic regularization term in the motion (8), which prevents the segmented surface to reach the contour if it is concave and with high curvature. However, the nuclei of not dividing cells are correctly segmented, as confirmed by visual inspection. Fig. 8 shows a complete sequence of an inner cell division. In the first stages the cell shape is irregular, because of the adhesion to its neighbors, but becomes spherical before mitosis. In the same way, the nucleus shape changes during cellular division from a spherical or ellipsoidal aspect to a more oblong and flat shape. These morphological features are linked to specific division phases.

1) *Prophase*: The nucleus starts changing its shape and gaining in intensity, because of chromosomes condensation, and the membrane gradually looses adhesion to the neighbors.
2) *Prometaphase*: Chromosomes attach to the mitotic spindle.
3) *Methaphase*: The chromosomes arrange in the future cell division plane.
4) *Anaphase*: The two sets of chromosomes separate;
5) *Telophase*: The membrane shows a constriction along the future cell division plane.
6) *Cytokinesis*: The daughter cells separate.

Eye inspection of the results reveals some problems in the segmentation of EVL membranes. As we described above, these cells surrounding the embryo are very flat. This feature impaired membrane completion by the Subjective Surfaces 3-D technique, because the small extension in depth stops the evolution process. Furthermore, EVL cells show intense intracellular labeling [as we can see in the central cell of Fig. 13(c)], probably corresponding to intracellular membrane compartments (Golgi
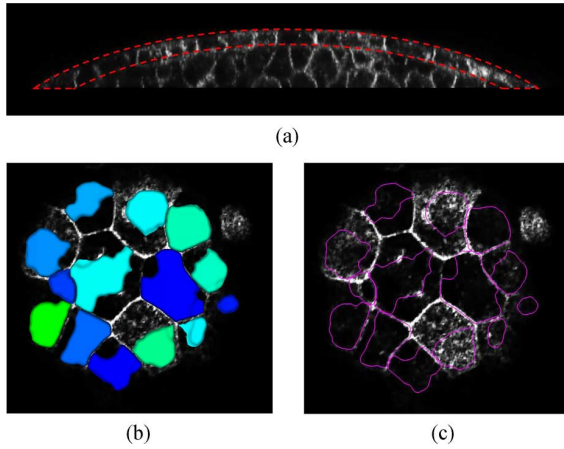
Fig. 13. Segmentation of epithelial cells: (a) location of the epithelial cells in the acquired volumes (dashed area), (b) segmented surfaces, (c) slice of the segmented surfaces superimposed on an image slice.
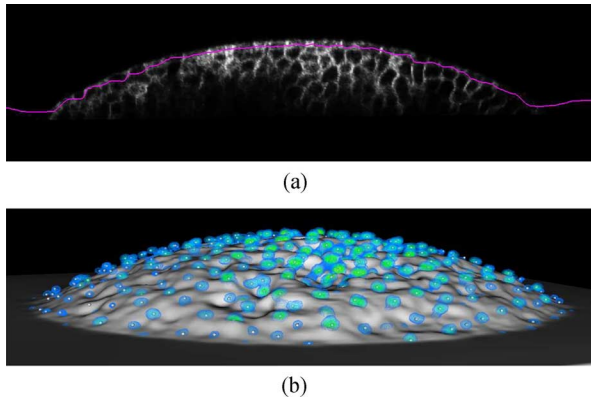

Fig. 14. Detection of the epithelial cells on a 3-D LMS dataset: (a) slice of the segmented surface, (b) superimposition of the segmented surface, nuclei channel in volume rendering representation and detected centers.
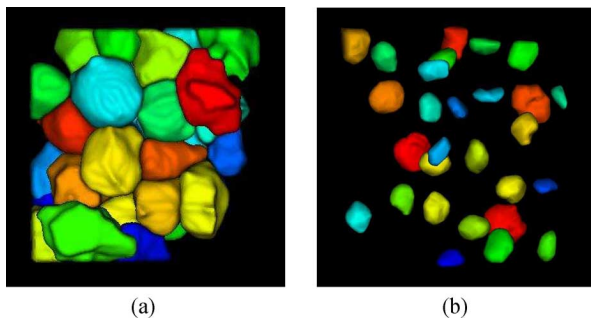

Fig. 15. Segmentation of an entire subvolume: (a) membranes, (b) nuclei.

apparatus or endoplasmic reticulum). When the evolving surface reaches this intracellular staining, it is not able to pass on. These considerations led us to think we require a specific method for the segmentation of the epithelial cells. Prior segmentation, they have to be automatically localized within the acquired volumes through a discriminating factor. At the moment, we are developing a simple method for the detection of the epithelial cells based on their position. First, we segment the surface of the embryo using the Geodesic Active Contours technique [36]. The evolution is not stopped by the external layer of

cells, because they have a weak outer contour, so we obtain the profile shown in Fig. 14(a). The epithelial cells remain outside [Fig. 14(b)] the surface and thus can be easily detected and classified as epithelial. This method is interesting because of its simpleness, but other factors could be used for the detection, such as the polygonal shape or the bigger size of epithelial nuclei. Finally, in Fig. 15, we show the segmentation of two subvolumes of nuclei and membranes. Every object is labeled with a different color, whose scalar value corresponds to the cell identity number.

VI. VALIDATION

In order to visually inspect the results validity, the segmentation algorithm has been first tested using a special framework designed for managing series of 3-D biological images [37]. The visual inspection of results allowed the detection of glaring mistakes in shape reconstruction, such as surfaces overlapping and incomplete contours. Nevertheless, this estimation is not enough to quantify the algorithm precision. We then designed a strategy to measure both the accuracy and robustness of our algorithm.

A. Accuracy Measurement

To estimate the accuracy we propose to measure the mismatch between a segmented surface and a gold standard obtained by manual segmentation. Such mismatch is quantified by using the *Hausdorff distance* and the *mean Hausdorff distance* [38], respectively associated to the maximum and mean segmentation error. In the foreseen validation method, the calculation of the distance should be repeated by considering different gold standards for the same membrane, to execute a statistical analysis on the data. This procedure should reduce the influence on results of the user who made the manual segmentation. The proposed procedure has been applied to a few cells and every manual segmentation has been performed with the tool ITK-Snap [39]. However, a first analysis on two cells with different shapes revealed interesting features (Table I). Cell1, imaged before division, is almost perfectly spherical, whereas cell2 has an irregular shape because of the adhesion to adjacent cells.

Examining different conformations, we want to estimate the effect of the "shape factor" on the algorithm precision. The mean Hausdorff distances are comparable for cell1: $0.4 \pm 0.2\,\mu$m and cell2: $0.3 \pm 0.0\,\mu$m. On the contrary, the maximum error is different whether the shape is spherical: $1.3 \pm 0.3\,\mu$m or irregular: $2.1 \pm 0.1\,\mu$m. These results suggest that the shape influences the maximum error but not the overall precision. This is probably due to the behavior already observed in Section V: The inability of the segmented surface to reach the contour if it is concave and with high curvature causes an increase of the maximum error in the irregular shapes (Fig. 16). Certainly, these results have to be supported by a larger record of cases. However, they indicate that our precision is at least sufficient to identify mitosis which is the major issue for further reconstructing cell behaviors.

B. Robustness Measurement

A robust segmentation method should correctly extract the shape of objects under different condition of image intensity, signal to noise ratio and image contrast. Due to the physics of

	H.d. (μm)	Mean H.d. (μm)
Cell1	1.3 ± 0.3	0.4 ± 0.2
Cell2	2.1 ± 0.1	0.3 ± 0.0

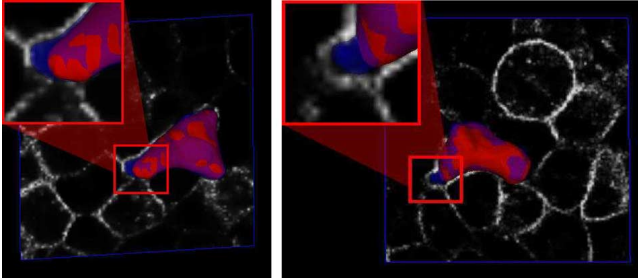| std	H.d. (μm)	Mean H.d. (μm)
50	1.2	0.3
100	1.6	0.5
150	2.6	0.8

Fig. 16. Details of segmented surfaces (red) and gold standards (blue) showing the region where the maximum segmentation error is located.
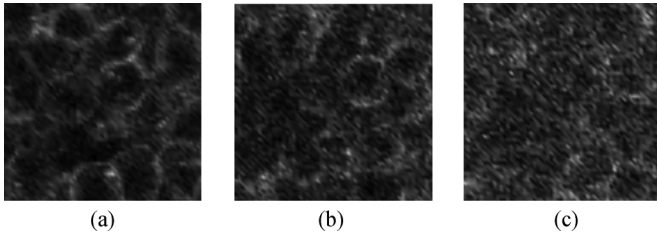

Fig. 17. Slices (xy plane) of membranes sub-volume at different depths of the sample. (a) Top. (b) Middle. (c) Bottom.
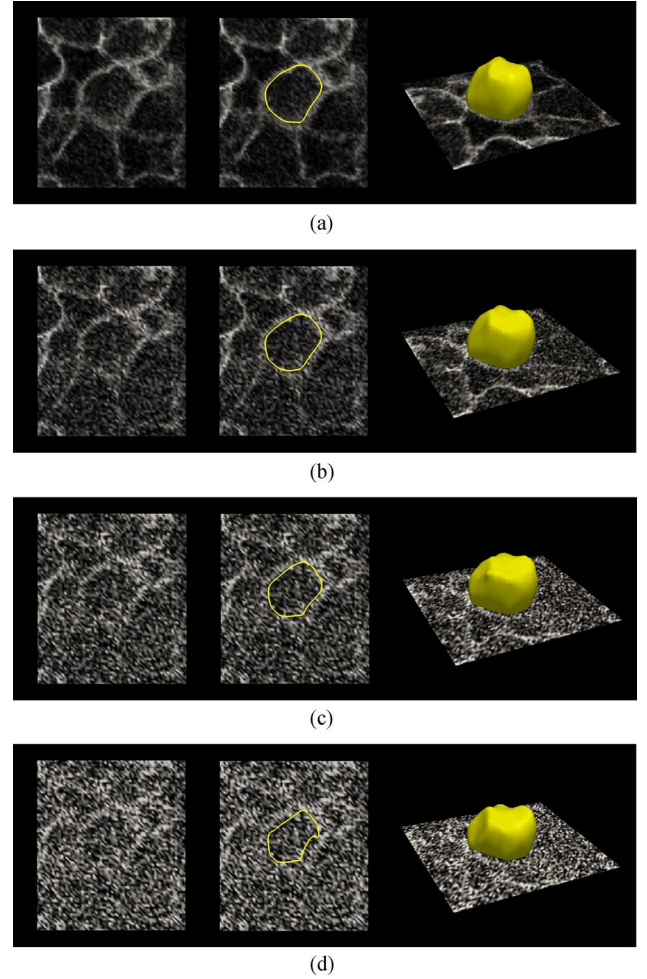

Fig. 18. Results of robustness procedure. Results of robustness procedure. Left: slices (xy plane) of the selected region. Middle: cut of segmented surfaces superimposed on the image slice. Right: segmented surfaces superimposed on the image slice. (a) Original data (gold standard). (b) Noisy data (std 50). (c) Noisy data (std 100). (d) Noisy data (std 150).

the acquisition process, our images are characterized by a signal to noise ratio which progressively decreases when moving in deep (z direction), as shown in Fig. 17.

Similar conditions can be achieved by artificially corrupting images with different levels of noise. Therefore, we aim at approaching a robustness measurement investigating whether our algorithm is able to segment a membrane enclosed in a region of interest which is progressively degraded by additive Gaussian noise. More precisely, the segmentation algorithm has been applied on three different images, attained by adding to the original a Gaussian noise with mean value zero and an increasing standard deviation of 50, 100, 150 [Fig. 18(b)–(d)]. We compared the segmentation results achieved on noisy images with the surface segmented on uncorrupted, original data, that in this case can be considered as gold standard [Fig. 18(a)]. Similarly to the accuracy estimation procedure, the mismatch between surfaces has been quantified through the use of the *Hausdorff distance* and the *mean Hausdorff distance* [38]. Our results, depicted in Table II and Fig. 18, clearly show that, despite the increment of noise influences the segmentation quality, however, in the worst case ($\text{std} = 150$) the mean and maximum error are respectively kept below $0.8\,\mu$m and $2.6\,\mu$m. Considering that in our scenario the voxel size is $0.58 \times 0.58 \times 1.04\,\mu\text{m}^3$ we can certainly assume that our algorithm is robust and its performances are acceptable even if applied on really corrupted images.

VII. CONCLUSION AND FUTURE WORKS

We designed an algorithm for the automated segmentation of membranes and nuclei based on Subjective Surfaces technique that has good performances on live zebrafish embryos confocal images. Visual inspection of the results has shown the ability of the algorithm to complete the missing contours, especially in membranes images, and to correctly reproduce the objects shape. Segmentation performances have been evaluated and quantified calculating the Hausdorff and the Mean Hausdorff distances between gold standard and segmented surfaces. With the proposed validation strategy we demonstrated that our algorithm performs well both in term of accuracy and robustness against noise. The local precision seems to decrease for

elongated and flat shapes (EVL cells and dividing nuclei). The algorithm could be improved by integrating the segmentation of membranes and nuclei, superimposing their edge indicators and defining two different isosurface values for extracting both shapes in the same process. A specific method could be designed for the segmentation of the EVL cells that have to be localized prior segmentation. With this work we have built the basis for future developments toward a deeper understanding of the biological processes involved in the organism formation. In this direction, the next step will be to pass the segmentation results to a specific algorithm for the cell shape analysis, that has to be defined yet, with the final goal to extract information on the cell state and analyze the dynamics of its shape.

REFERENCES

[1] P. J. Keller, A. D. Schmidt, J. Wittbrodt, and E. H. Stelzer, "Reconstruction of zebrafish early embryonic development by scanned light sheet microscopy," *Science*, vol. 322, pp. 1065–1069, 2008.

[2] S. J. Lockett and B. Herman, "Automatic detection of clustered, fluorescence-stained nuclei by digital image-based cytometry," *Cytometry*, vol. 17, pp. 1–12, 1994.

[3] A. I. Dow, J. M. Shafer, J. M. Kirkwood, R. A. Mascari, and A. S. Waggoner, "Automatic multiparameter florescence imaging for determining lymphocyte phenotype and activation status in Melanoma tissue sections," *Cytometry*, vol. 25, pp. 71–81, 1996.

[4] N. Malpica, C. Ortiz de Solorzano, J. J. Vaquero, A. Santos, I. Vallcorba, J. M. Garcia-Sagredo, and F. del Pozo, "Applying watershed algorithms to the segmentation of clustered nuclei," *Cytometry*, vol. 28, pp. 289–297, 1997.

[5] J. P. Rigaut, J. Vassy, P. Herlin, F. Duigou, E. Masson, D. Briane, J. Foucrier, S. Carvajal-Gonzalez, A. M. Downs, and A. M. Mandard, "Three-dimensional DNA image cytometry by confocal scanning laser microscopy in thick tissue blocks," *Cytometry*, vol. 12, pp. 511–524, 1991.

[6] T. Irinopoulou, J. Vassy, M. Beil, E. Nicopoulou, D. Encaoua, and J. P. Rigaut, "Three-dimensional DNA image cytometry by confocal scanning laser microscopy in thick tissue blocks of prostatic lesions," *Cytometry*, vol. 27, pp. 99–105, 1997.

[7] K. Rodenacker, M. Aubele, P. Hutzler, and P. S. Umesh Adiga, "Groping for quantitative digital 3-D image analysis: An approach to quantitative in situ hybridization in thick tissue sections of prostate carcinoma," *Anal. Cell. Pathol.*, vol. 15, pp. 19–29, 1997.

[8] S. J. Lockett, D. Sudar, C. T. Thompson, D. Pinkel, and J. W. Gray, "Efficient, interactive, three-dimensional segmentation of cell nuclei in thick tissue sections," *Cytometry*, vol. 31, pp. 275–286, 1998.

[9] C. Ortiz de Solorzano, E. Garcia Rodriguez, A. Jones, D. Pinkel, J. W. Gray, D. Sudar, and S. J. Lockett, "Segmentation of confocal microscope images of cell nuclei in thick tissue section," *J. Microsc.*, vol. 193, pp. 212–226, 1999.

[10] A. Sarti, C. Ortiz de Solorzano, S. Lockett, and R. Malladi, "A geometric model for 3-D confocal image analysis," *IEEE Trans. Biomed. Eng.*, vol. 47, pp. 1600–1609, 2000.

[11] D. R. Padfield, J. Rittscher, T. Sebastian, N. Thomas, and B. Roysam, "Spatio-temporal cell cycle analysis using 3D level set segmentation of unstained nuclei in line scan confocal fluorescence images," in *Proc. 3rd IEEE Int. Symp. Biomedical Imaging: Nano to Macro*, 2006, pp. 1036–1039.

[12] X. Wang, W. He, D. Metaxas, R. Mathew, and E. White, "Cell segmentation and tracking using texture-adaptive snakes," in *Proc. 4th IEEE Int. Symp. Biomedical Imaging: From Nano to Macro*, 2007, pp. 101–104.

[13] C. Ortiz de Solorzano, R. Malladi, S. A. Leliévre, and S. J. Lockett, "Segmentation of nuclei and cells using membrane related protein markers," *J. Microsc.*, vol. 201, pp. 404–415, 2001.

[14] A. Sarti, R. Malladi, and J. A. Sethian, "Subjective surfaces: A method for completing missing boundaries," *Proc. Nat. Acad. Sci. United States of America*, vol. 12, pp. 6258–6263, 2000.

[15] A. Sarti and G. Citti, "Subjective surfaces and Riemannian mean curvature flow of graphs," *Acta Math. Univ. Comenianae*, vol. LXX, no. 1, pp. 85–103, 2001.

[16] A. Sarti, R. Malladi, and J. A. Sethian, "Subjective surfaces: A geometric model for boundary completion," *Int. J. Comput. Vis.*, vol. 46, pp. 201–221, 2002.

[17] C. Zanella, B. Rizzi, C. Melani, M. Campana, P. Bourgine, K. Mikula, N. Peyriéras, and A. Sarti, "Segmentation of cells from 3D confocal images of live Zebrafish embryo," in *Proc. IEEE Eng. Med. Biol. Soc.*, 2007, pp. 6027–6030.

[18] S. Megason and S. Fraser, "Digitizing life at the level of the cell: High-performance laser-scanning microscopy and image analysis for in toto imaging of development," *Mech. Dev.*, vol. 120, pp. 1407–1420, 2003.

[19] K. Dooley and L. Zon, "Zebrafish: A model system for the study of human disease," *Curr. Opin. Genet. Dev.*, vol. 10, no. 3, pp. 252–256, 2000.

[20] C. B. Kimmel, W. W. Ballard, S. R. Kimmel, B. Ullmann, and T. F. Schilling, "Stages of embryonic development of the zebrafish," *Dev. Dyn.*, vol. 203, pp. 253–310, 1995.

[21] Z. Kriva, K. Mikula, N. Peyriéras, B. Rizzi, and A. Sarti, "3D early embryogenesys image filtering by nonlinear partial differential equations," *Med. Image Anal.*, submitted for publication.

[22] B. Rizzi, M. Campana, C. Zanella, C. Melani, R. Cunderlik, Z. Kriva, P. Bourgine, K. Mikula, N. Peyriéras, and A. Sarti, "3D zebra fish embryo images filtering by nonlinear partial differential equations," in *Proc. IEEE Eng. Med. Biol. Soc.*, 2007, pp. 6251–6254.

[23] V. Caselles, R. Kimmel, and G. Sapiro, "Geodesic active contours," *Int. J. Comput. Vis.*, vol. 22, pp. 61–79, 1997.

[24] R. Malladi, J. A. Sethian, and B. C. Vemuri, "Shape modeling with front propagation: A level set approach," *IEEE Trans. Pattern Anal. Mach. Intell.*, vol. 17, pp. 158–175, 1995.

[25] P. Perona and J. Malik, "Scale-space and edge detection using anisotropic diffusion," *IEEE Trans. Pattern Anal. Mach. Intell.*, vol. 12, pp. 629–639, 1990.

[26] D. Ballard, "Generalizing the hough transform to detect arbitrary shapes," *Pattern Recognit.*, vol. 13, pp. 111–122, 1981.

[27] C. Melani, M. Campana, B. Lombardot, B. Rizzi, F. Veronesi, C. Zanella, P. Bourgine, K. Mikula, N. Peyriéras, and A. Sarti, "Cells tracking in a live zebrafish embryo," in *Proc. IEEE Eng. Med. Biol. Soc.*, 2007, pp. 1631–1634.

[28] J. Canny, "A computational approach to edge detection," *IEEE Trans. Pattern Anal. Mach. Intell.*, vol. PAMI-8, no. 6, pp. 679–698, Jun. 1986.

[29] L. C. Evans and J. Spruck, "Motion of level sets by mean curvature I," *J. Diff. Geom.*, vol. 33, pp. 635–681, 1991.

[30] S. Osher and J. A. Sethian, "Front propagating with curvature dependent speed: Algorithms based on Hamilton Jacobi formulation," *J. Comput. Phys.*, vol. 79, pp. 12–49, 1988.

[31] R. J. LeVeque, *Finite Volume Methods for Hyperbolic Problems*. Cambridge, MA: Cambridge Univ. Press, 2002.

[32] K. Mikula and N. Ramarosy, "Semi-implicit finite volume scheme for solving nonlinear diffusion equations in image processing," *Numer. Math.*, vol. 89, no. 3, pp. 561–590, 2001.

[33] S. Corsaro, K. Mikula, A. Sarti, and F. Sgallari, "Semi-implicit co-volume method in 3D image segmentation," *SIAM J. Sci. Comput.*, vol. 28, no. 6, pp. 2248–2265, 2006.

[34] K. Mikula, A. Sarti, and F. Sgallari, "Co-volume level set method in subjective surface based medical image segmentation," in *Handbook of Medical Image Analysis: Segmentation and Registration Models*, J. Suri, Ed. *et al.* New York: Springer, 2005, pp. 583–626.

[35] K. Mikula, A. Sarti, and F. Sgallari, "Co-volume method for Riemannian mean curvature flow in subjective surfaces multiscale segmentation," *Comput. Vis. Sci.*, vol. 9, no. 1, pp. 23–31, 2006.

[36] V. Caselles, R. Kimmel, and G. Sapiro, "Geodesic active contours," *Int. J. Comput. Vis.*, vol. 22, pp. 61–79, 1997.

[37] M. Campana, B. Rizzi, C. Melani, P. Bourgine, N. Peyriéras, and A. Sarti, "A framework for 4D-biomedical image processing, visualization and analysis," in *Proc. 3rd Int. Conf. Computer Graphics Theory and Applications*, 2008, pp. 403–408.

[38] J. W. Zhang, G. Q. Han, and Y. Wo, "Image registration based on generalized and mean hausdorff distances," in *Proc. 4th Int. Conf. Machine Learning and Cybernetics*, 2005, pp. 5117–5121.

[39] P. A. Yushkewich, J. Piven, H. C. Hazlett, R. G. Smith, S. Ho, J. C. Gee, and G. Gerig, "User guided 3D active contour segmentation of anatomical structures: Significantly improved efficiency and reliability," *Neuroimage* vol. 31, pp. 1116–1128, 2006 [Online]. Available: http://www.itksnap.org

Gonzalo Sanguinetti received the E.E. degree in 2005 from the Universidad de la Repblica, Montevideo, Uruguay, where he is currently pursuing the doctoral degree in electrical engineering.

He is also a visiting student at the University of Bologna, Bologna, Italy.

Paul Bourgine received the Ph.D. degree in economics and cognitive science.

He is the Director of CREA-Ecole Polytechnique and of the National Network on Complex Systems. His scientific interests include complex adaptive systems and large interactive networks. His current research fields include genetic networks, neural networks, social networks and social cognition, learning, and co-evolutionary dynamics.

Dr. Bourgine was the Co-Chair of the first two Conferences in Economics and Artificial Intelligence (CECOIA 1986, 1990), the first European Conference of Artificial Life (ECAL 1990), the first European Conference in Cognitive Economics (ECCE 2004), and Chair of the European Conference on Complex Systems (ECCS'05).

Cecilia Zanella received the B.S. degree in 2004 and the M.S. degree in 2006 in biomedical engineering from Bologna University, Bologna, Italy.

She is currently collaborating with the Department of Electronics, Computer Sciences and Systems (DEIS), Bologna, for the development of image processing based projects. Her research interests are biomedical and biological image processing and image analysis.

Karol Mikula received the Ph.D. degree in numerical analysis in 1993 from Comenius University, Bratislava, Slovakia.

He is currently a Full Professor of applied mathematics at the Slovak University of Technology, Bratislava. His research interests are focused on numerical analysis of nonlinear partial differential equations and applications in various fields of science and technology including large scale image processing.

Matteo Campana received the B.S. degree in electronic engineering in 2001 and the M.S. degree in information and communication technologies in 2006 from Bologna University, Bologna, Italy. He is currently pursuing the Ph.D. degree in bioengineering at the Department of Electronics, Computer Sciences and Systems (DEIS), Bologna.

His research interests are biomedical and biological image processing, image analysis, and scientific visualization.

Nadine Peyriéras received the Ph.D. degree at the Pasteur Institute, France, in 1986 on the characterization of cell adhesion molecules in mice.

After postdoctoral training on mouse brain development (IBDM, Marseille, France) and mesendoderm formation in zebrafish (ENS, Paris, France), she established her own team in 2002 at Paris 6 University on midline formation in Deuterostomians. In 2006, she established and coordinated the EU project Embryomics (NEST adventure) in Gif-sur-Yvette (CNRS), France, providing the first automated and controlled strategies to achieve the reconstruction of the cell lineage tree in Deuterostomians (http://www.embryomics.eu).

Barbara Rizzi received the M.S. degree in biomedical engineering in 2005 and the Ph.D. degree in bioengineering in 2009 from the University of Bologna, Italy.

She is currently collaborating with the CREA, Paris, France. Her research interests include biomedical and biological image processing and analysis.

Alessandro Sarti received the M.S. degree in electronic engineering in 1991 and the Ph.D. degree in bioengineering, with a thesis in computational image analysis, in 1996 from the University of Bologna, Bologna, Italy.

In 1997, he took a postdoctoral position at the Mathematics Department, University of California, Berkeley, and the Lawrence Berkeley National Laboratory, University of California, Berkeley. He is currently a Research Professor of Bioengineering, University of Bologna. His research interests include biologically based vision, computer vision, biomedical image processing, and image analysis.

Camilo Melani was born in Cordoba, Argentina, in 1978. He received the B.Sc. and the M.Sc. degrees in computer science from the Universidad de Buenos Aires, Argentina, in 2004, where he is currently pursuing the doctoral degree in computer science.

He is also a visiting student at the University of Bologna, Bologna, Italy, and ISCPIF CNRS, Paris, France.